
Volume 1 | Number 1 | Jan 2013 | Pages 1–100
PCCP
Physical Chemistry Chemical Physics
www.rsc.org/pccp
ROYAL SOCIETY OF CHEMISTRY

Cite this: DOI: 10.1039/c0xx00000x

www.rsc.org/xxxxxx

ARTICLE TYPE

$Ba_5\{V,Nb\}_{12}Sb_{19+x}$, Novel Variants of the $Ba_5Ti_{12}Sb_{19+x}$ - type: Crystal Structure and Physical Properties

F. Failamani[a,b], A. Grytsiv[a,f], G. Giester[c], G. Polt[d], P. Heinrich[e], H. Michor[e], E. Bauer[e,f], M. Zehetbauer[d], P. Rogl[a,f,♣]

Received (in XXX, XXX) Xth XXXXXXXXX 20XX, Accepted Xth XXXXXXXXX 20XX
DOI: 10.1039/b000000x

The novel compounds $Ba_5\{V,Nb\}_{12}Sb_{19+x}$, initially found in diffusion zone experiments between Ba-filled skutterudite $Ba_{0.3}Co_4Sb_{12}$ and group V transition metals (V,Nb,Ta), were synthesized via solid state reaction and were characterized by means of X-ray (single crystal and powder) diffraction, electron probe microanalysis (EPMA), and physical (transport and mechanical) properties measurements. $Ba_5V_{12}Sb_{19.41}$ (a=1.21230(1) nm, space group $P\bar{4}3m$; R_{F2}=0.0189) and $Ba_5Nb_{12}Sb_{19.14}$ (a=1.24979(2) nm, space group $P\bar{4}3m$; R_{F2}=0.0219) are the first representatives of the $Ba_5Ti_{12}Sb_{19+x}$-type, however, in contrast to the aristotype, the structure of $Ba_5V_{12}Sb_{19.41}$ shows additional atom disorder. Temperature dependent ADPs and specific heat of $Ba_5V_{12}Sb_{19.41}$ confirmed the rattling behaviour of Ba1,2 and Sb7 atoms within the framework built by V and Sb atoms. Electrical resistivity of both compounds show an upturn at low temperature, and a change from p- to n-type conductivity above 300 K in $Ba_{4.9}Nb_{12}Sb_{19.4}$. As expected from the complex crystal structure and the presence of defects and disorder, the thermal conductivity is suppressed and lattice thermal conductivity of ~0.43 W/m.K is near values typical for amorphous systems. Vicker's hardness of (4.1±0.1) GPa (vanadium compound) and (3.6±0.2) GPa (niobium compound) are comparable to Sb-based filled skutterudites. However, the indentation Young's moduli for these compounds $E_I(Ba_{4.9}V_{12}Sb_{19.0})$ = (85±2) GPa and $E_I(Ba_{4.9}Nb_{12}Sb_{19.4})$ = (79±5) GPa are significantly smaller than those of skutterudites, which range at about 130 to 145 GPa.

♣ Corresponding author; email: peter.franz.rogl@univie.ac.at

Cite this: DOI: 10.1039/c0xx00000x

www.rsc.org/xxxxxx

ARTICLE TYPE

1. Introduction

Ternary compounds from the systems EP-M-Sb, combining electropositive elements (EP = alkaline and alkaline earth metals) and early transition metals M, are rare cases among ternary antimonides. Practically complete immiscibility between these two groups of metals [1,2] indicates that bonding interactions are unlikely. The binary immiscibility, together with the high vapor pressure of group I and II metals and antimony also makes preparation routes rather difficult. Hitherto Li and Ba are the only known alkaline and alkaline earth metals that form antimonides with early transition metals. Compounds within the systems Li-M-Sb (M = Ti, V, Zr, Hf) are mostly based on binary Li-Sb phases where the transition metals substitute for Li atoms. Whilst various ternaries Li-M-Sb are known,[2] so far only one compound, $Ba_5Ti_{12}Sb_{19+x}$, has been identified among the systems Ba-M-Sb.[3] The crystal structure of $Ba_5Ti_{12}Sb_{19+x}$ can be considered as a combination of ordered γ-brass subunits (Cu_9Al_4-type) formed by Ba and Sb atoms and a 3D Ti network. It is interesting to note that this compound crystallizes in a non-centrosymmetric space group, $P\bar{4}3m$.

On the other hand, our thermoelectric (TE) research on Ba-filled skutterudites demands also the search for suitable electrode materials and/or diffusion barriers at the hot side of a thermoelectric generator device. Electrode materials should provide good electrical and thermal transport, high mechanical stability and small differences in thermal expansion with the p- and n- type TE materials. For thermoelectric generators in temperature gradients from 300 to 900 K, skutterudites have shown to provide a thermoelectric leg efficiency reaching 15% and device efficiency with commercial TE material of 8 %.[4–11] Long term stability in TE devices, however, requests chemical compatibility of the hot electrode (mainly Ni or Cu) with the thermoelectric material. Severe interaction of n- and p-type skutterudites with late 3d-metal electrodes (formation of antimonides) must be prevented by diffusion barriers. Almost complete immiscibility between early transition metal elements and earth alkaline filler atoms, together with a coefficient of thermal expansion close to the average of filled skutterudites, [12] suggest suitability of early transition metals for such applications. Several reports can be found regarding the use of early transition metal elements (mainly Ti) as diffusion barrier for TE skutterudites and Ni,Cu electrodes.[13,14] In our attempts to explore the potential of group V transition metals (V, Nb, Ta) as barriers, diffusion zone experiments between Ba-filled skutterudite $Ba_{0.3}Co_4Sb_{12}$ and (V,Nb,Ta) revealed the formation of a novel ternary compound with vanadium, the formula of which being close to a 5-12-20 stoichiometry (see Figure 1; for details on the binary phase diagrams {V,Nb,Ta}-Sb see ref. [15]).

The present paper will thus focus on (i) the exploration of phase formation and crystal structure in the ternary systems Ba-{V,Nb,Ta}-Sb particularly for compounds $Ba_5\{V,Nb,Ta\}_{12}Sb_{19+x}$, (ii) on the evaluation of their physical properties, and (iii) on the suitability of V, Nb, Ta metals as a diffusion barrier for the hot electrode in a TE-generator based on Ba-filled skutterudites.

2. Experimental Methods

Alloys were prepared from Ba rods (Alfa Ventron, 99+, <0.8 mass% Sr), antimony chunks (Alfa Ventron, 99.9%), vanadium pieces (Vanadium Corporation, 99.71%), and niobium/tantalum powders (325 mesh, Sigma Aldrich, 99.9%). First $\{V,Nb,Ta\}Sb_x$ master alloys were made either by arc melting (in case of vanadium) or by synthesis from powder mixtures at 900°C in sealed quartz vials (niobium/tantalum). In a second step, barium pieces were arc melted together with proper amounts of the $\{V,Nb,Ta\}Sb_x$ master alloys. Due to the high vapor pressure and the highly exothermic interaction between Ba and Sb, and a practically complete immiscibility in the Ba-{V,Nb,Ta} systems, it was not possible to reliably assign the weight losses. After several trial and errors single phase bulk samples $Ba_5\{V,Nb\}_{12}Sb_{19+x}$ for property measurements were obtained by solid state reaction of powder compacts of $BaSb_3$, Sb, Nb and powder of a V-rich VSb_x master alloy. All powders were handled inside an Ar-filled glovebox with O_2 and water vapor levels below 5 ppm. $BaSb_3$ master alloys were prepared via vapor transport between Ba pieces and Sb pieces at 500°C, while VSb_x master alloys were prepared by direct arc melting of V and Sb pieces. All master alloys were powderized and sieved below a grain size of 150 μm prior to mixing with other constituents. Stoichiometric blends of these constituents then were ball milled under argon for two hours in a Fritsch Vario-planetary mill PULVERISETTE 4 (in tungsten carbide vessels with tungsten carbide balls) in order to increase the surface area and to homogenize the mixtures. Ball milled powders were then loaded within the glove box into graphite dies and hot pressed in an FCT uniaxial hot press system HP W 200/250 2200-200-KS at 500°C for three hours under a pressure of 38 MPa. Each billet was then surface cleaned, vacuum sealed in a quartz ampoule and annealed for 2 weeks at 700°C for V and 900°C for Nb. The annealed alloys were re-powderized and sieved below 53 μm grain size and hot pressed in the same equipment at 50 MPa and the same temperature as for the annealing process. The relative density of the hot pressed sample could only be determined by the Archimedes' method for the Nb compound (~ 96% of the theoretical density). All alloys were analyzed by X-ray powder diffraction with Ge-monochromated $CuK\alpha_1$-radiation employing a Guinier-Huber image plate recording system. Rietveld refinements were performed using the program FullProf,[16] while precise lattice parameters were obtained by least squares fit methods with the program STRUKTUR [17] employing Ge/Si as internal standards (a_{Ge}= 0.5657906 nm; a_{Si}= 0.5431065 nm). Quantitative elemental analyses were performed by SEM on a Zeiss Supra 55 VP equipped with an energy dispersive X-ray (EDX) detector operated at 20 kV. Samples for EPMA were

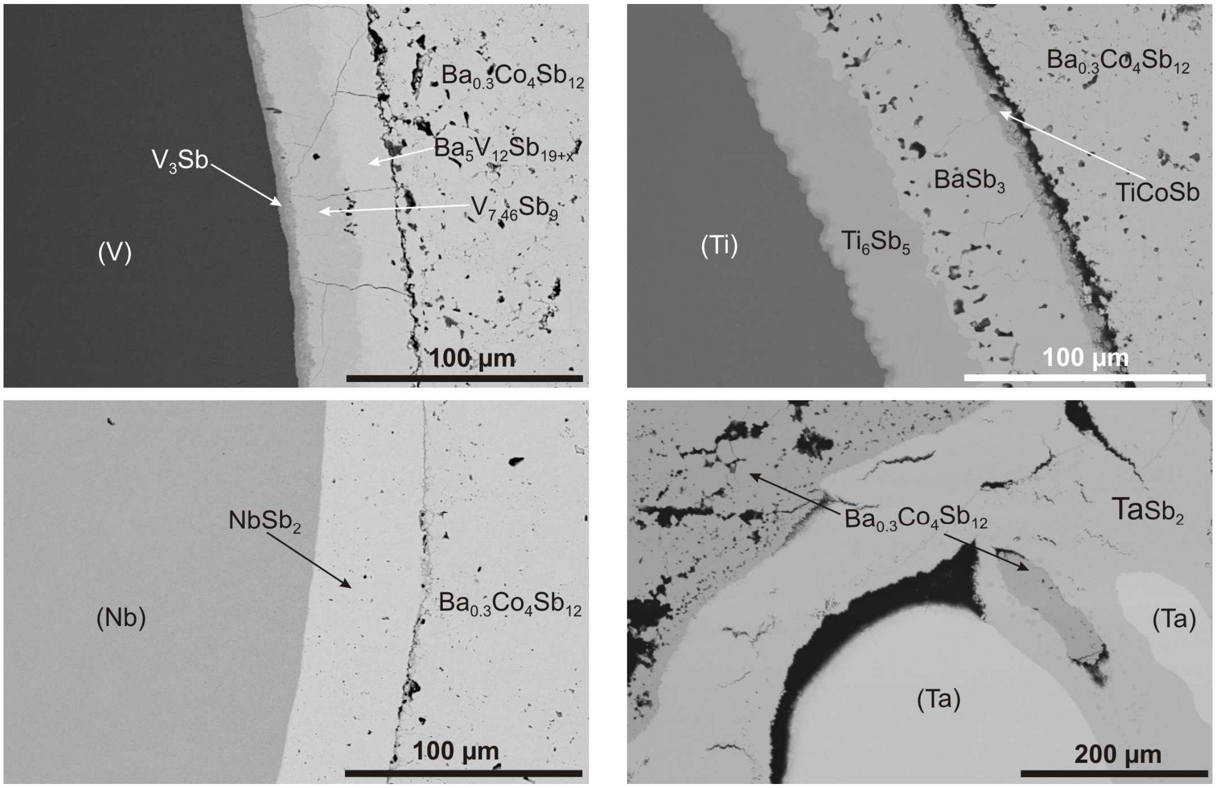

Figure 1. Diffusion zones formed between n-type $Ba_{0.3}Co_4Sb_{12}$ and group-V metals (V,Nb,Ta) and Ti at 600°C annealed for 40 days.

prepared by standard metallographic methods. In some cases polishing was performed under glycerine instead of water to avoid oxidation and/or hydrolysis of samples, especially for Ba-rich alloys.

Single crystals of $Ba_5V_{12}Sb_{19+x}$ suitable for X-ray structure analysis were grown from alloys arc melted under argon with nominal composition of Ba12V29Sb59 (in at.%) in equilibrium with Sb-rich liquid annealed at 650°C for 5 weeks. Single crystals of $Ba_5Nb_{12}Sb_{19+x}$ were obtained from two alloys (nominal composition: Ba25Nb15Sb60 and Ba30Nb14Sb56) in equilibrium with Ba-rich liquid at 900°C. In all cases rather "spherical" single crystal fragments with "diameters" in the range of 30 to 60 µm were mechanically isolated from the crushed alloys. Inspections on an AXS D8-GADDS texture goniometer assured high crystal quality, unit cell dimensions and Laue symmetry of the single crystal specimens prior to X-ray intensity data collections at room temperature on a four-circle Nonius Kappa diffractometer equipped with a CCD area detector employing graphite monochromated MoKα radiation (λ = 0.071069 nm) whereby constant temperatures for the crystal, mounted with transparent varnish on a glass rod, were assured by a continuous stream of nitrogen gas enclosing the crystal at preset temperature. Orientation matrices and unit cell parameters were derived using the program DENZO.[18] Besides psi-scans no additional absorption corrections were performed because of the rather regular crystal shapes and small dimensions of the investigated specimens. The structures were solved by direct methods (SHELXS-97) and were refined with the SHELXL-97 [19] program within the Windows version WinGX. [20] Crystal structure data were standardized using program STRUCTURE-TIDY.[21]

Attempts to adopt the same procedures to produce either single crystals or single-phase $Ba_5Ta_{12}Sb_{19+x}$ did not yield any significant amount of this phase.

Both samples, $Ba_5\{V,Nb\}_{12}Sb_{19+x}$, possess a high degree of brittleness, however, in case of $Ba_5Nb_{12}Sb_{19+x}$ careful processing of the hot pressed sample allowed us to obtain a specimen large enough for various physical properties measurement. Due to the extreme brittleness of the $Ba_5V_{12}Sb_{19+x}$ sample, the same procedures did not work, as the hot pressed sample tends to shatter easily during the post hot pressing processes, e.g. removal from die, grinding, and cutting. Therefore only low temperature electrical resistivity, specific heat and hardness measurements could be performed for this compound.

Low temperature resistivity measurements were carried out by a standard four-probe a.c. bridge technique in a home made equipment from 2 - 300 K, whereas the high temperature data (300 - 823 K) together with Seebeck coefficient were measured simultaneously with an ULVAC-ZEM3 instrument. Due to small sample size of $Ba_5V_{12}Sb_{19+x}$ (~3 mm in length), contacts for electrical resistivity measurement were made using thin gold wire (ø = 50 µm). The spot welded contacts then were coated with silver epoxy in order to improve their mechanical stability. Specific heat measurements were performed on a commercial Quantum Design PPMS calorimeter for $Ba_5V_{12}Sb_{19+x}$ (~50 mg sample mass) and on a homemade calorimeter with adiabatic step heating technique for $Ba_5Nb_{12}Sb_{19+x}$ (~1.8 g sample mass).[22–24] Hardness and elastic moduli were obtained by nano-indentation (ASMEC-UNAT) with a Berkovic indenter employing a quasi-continuous stiffness measurement method in a range of loads from 20 to 100 mN.

3. Results and discussion

3.1. Structure solution and refinement

3.1.1. The crystal structure of $Ba_5V_{12}Sb_{19+x}$

Complete indexation of the X-ray single crystal diffraction data prompted a primitive cubic unit cell with lattice parameter a=1.21230(1) nm. Systematic analysis of extinctions suggested $Pm\bar{3}m$, $P\bar{4}3m$, $P\bar{4}32$, $Pm\bar{3}$, and $P23$ as possible space group types. Searching in the Pearson crystal database[2] for structure types with similar unit cell and Pearson symbol (derived from unit cell and EPMA data) prompted one entry, $Ba_5Ti_{12}Sb_{19+x}$, with a similar XRPD pattern as our phase. Indeed structure solution and refinement in the non-centrosymmetric space group $P\bar{4}3m$ revealed an atomic arrangement as in $Ba_5Ti_{12}Sb_{19+x}$, however, with a large electron density of ~65×10^3 e$^-$/nm^3 at (½,½,½). Taking into account the distance between this peak and the nearest neighbouring atoms, this residual electron density was assigned to a partial occupation of Sb (atom Sb7), which refined to an occupancy occ(Sb7) ~ 0.5. At this stage the residual electron density map (see Figure 2) prompted two further significant electron densities of ~25×10^3 e$^-$/nm^3, at very close distance (~0.04 nm) to Ba1 (~0.18,½,½) resulting in an ellipsoidal electron density for Ba1, eventually indicating a split position for Ba1. Splitting Ba1 into two positions (assigned as Ba*1a* (~0.17,½,½) and Ba*1b* (~0.20,½,½) significantly improved the R-factor (R_{F2} = 0.031) and without any constraint the occupancy of each split position refined to almost equal values (occ~0.5), with a slightly smaller value for Ba*1a*.

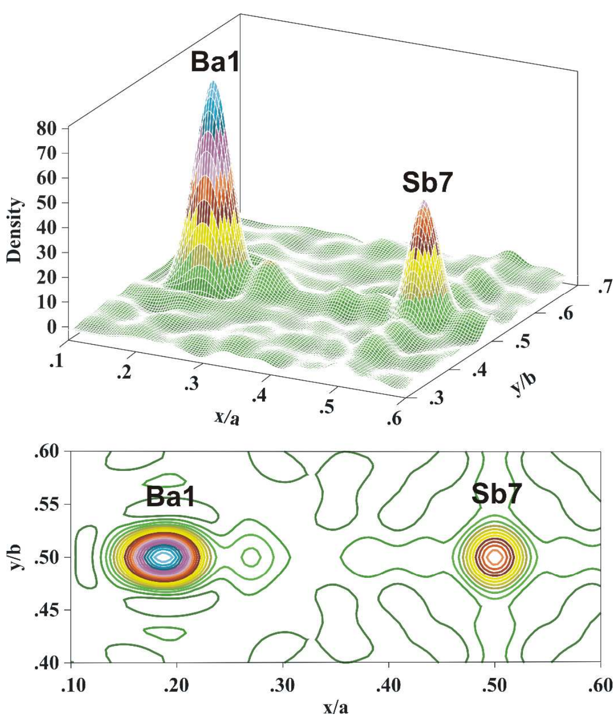

Figure 2. Difference Fourier map of $Ba_5V_{12}Sb_{19+x}$ at z=0.5 around Ba1 from data measured at 100 K.

At this stage of refinement, a rather small residual electron density of ~7×10^3 e$^-$/nm^3 at (~0.46,~0.46,~0.46) was still unassigned, which is very close (~0.08 nm) to the partially occupied Sb7 site. The distances from this peak to the next nearest neighbour atoms Sb5 (0.30 nm) and Ba*1b* (0.32 nm) correspond very well to the sum of Ba-Sb and Sb-Sb radii [25]. A similar situation was also observed by Bie and Mar [3] in $Ba_5Ti_{12}Sb_{19+x}$, where a residual density of 7.1×10^3 e$^-$/nm^3 was observed and was initially thought to be an oxygen atom. Following the arguments from Bie and Mar [3] regarding the interatomic distances of this peak to the nearest neighbours, the residual electron density was finally assigned to a partial occupation of Sb6 in this position (refined to occ(Sb6)~0.07). The low occupancies of Sb6 (occ.~0.07) and of Sb7 (occ.~0.50) may safely rule out that both atoms are simultaneously present in the structure.

The final refinement, assigning anisotropic ADP's to all atoms except Ba*1a* and Ba*1b*, resulted in R_{F2} = 0.0189, now with acceptably low residual electron densities of 3.83/-1.57×10^3 e$^-$/nm^3. An alternative structural model employing 3 split positions for Ba1 (Ba*1a*, Ba*1b* and Ba*1c*), resulted in only a slightly lower R_{F2} = 0.0167 and smaller residual electron density of 2.74/-1.16 ×10^3 e$^-$/nm^3 and thus provides no significant improvement. The final formula from refinement, $Ba_5V_{12}Sb_{19.4}$ (≡ $Ba_{13.4}V_{33.1}Sb_{53.5}$), agrees well with the composition derived from EPMA ($Ba_{13.3}V_{33.7}Sb_{53.0}$ in at. %). Results are summarized in Table 1; interatomic distances are presented in Table 2. We want to note here, that for easy comparison we have kept atom labels and site parameters consistent with the standardized description of the parent structure of $Ba_5Ti_{12}Sb_{19+x}$.[3] For a detailed description of the crystal structure of $Ba_5V_{12}Sb_{19.4}$ see Section 3.2.

X-ray powder Rietveld refinement for the sample, which supplied the single crystal, is consistent with the structural model obtained from X-ray single crystal refinement. The disorder, however, could not be reliably extracted, therefore the occupancy values of Ba1a/b, Sb6, and Sb7 were fixed according to the single crystal refinement data. The Flack parameters for all models are close to 0; therefore we may conclude the presence of only one absolute configuration. A test for higher symmetry, employing program PLATON, confirmed that no symmetry is missing for the crystal structure data, in good agreement with the result from the E-test yielding only 31% probability for centrosymmetry.

3.1.2. The crystal structure of $Ba_5Nb_{12}Sb_{19+x}$

The discovery of $Ba_5V_{12}Sb_{19+x}$ led us to search for homologous and isotypic compounds $Ba_5M_{12}Sb_{19+x}$ with M = Zr, Hf, Nb, Ta, Cr, Mo, W, of which Nb and Ta, indeed, were found to form corresponding phases in alloys annealed at 700°C for 7 days (see Figure 3; for details on the binary phase diagrams {Nb,Ta}-Sb see ref. [15]). The formation of $Ba_5Nb_{12}Sb_{19+x}$ was confirmed by both XRPD and XRSC data. But we were unable to either synthesize bulk $Ba_5Ta_{12}Sb_{19+x}$ or to extract suitably sized single crystals for X-ray structure determination.

Despite a single-phase sample $Ba_5Nb_{12}Sb_{19+x}$ could be obtained by powder metallurgical reaction synthesis, it deemed necessary to provide X-ray single crystal data in order to unambiguously identify atom disorder and partial occupancy as for $Ba_5V_{12}Sb_{19+x}$. In contrast to the single crystal of $Ba_5V_{12}Sb_{19+x}$, which was grown from equilibrium with a Sb-rich liquid, such an equilibrium does not exist in the Ba-{Nb,Ta}-Sb ternary systems, neither at 700° nor at 900°C. Therefore a single crystal of $Ba_5Nb_{12}Sb_{19+x}$ was grown from the equilibrium with a Ba-rich liquid annealing for two weeks at 900°C. EPM analysis proved that no foreign elements were present in the $Ba_5Nb_{12}Sb_{19+x}$ phase. Diffraction data from a single crystal suitable for X-ray structure determination were completely indexed on a unit cell similar to $Ba_5V_{12}Sb_{19+x}$. Considering isotypism, structure solution and refinement were successfully performed in the non-centrosymmetric space group type $P\bar{4}3m$ with $Ba_5Ti_{12}Sb_{19+x}$ as initial structure model.

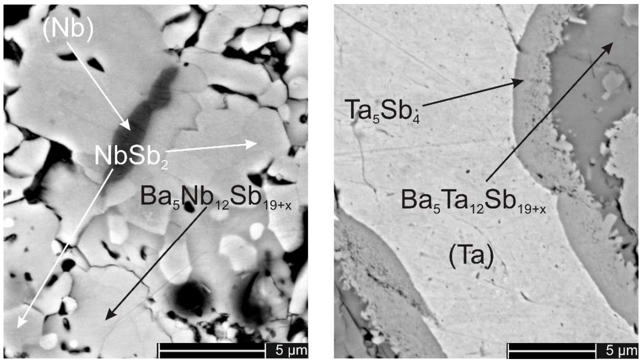

Figure 3. $Ba_5\{Nb,Ta\}_{12}Sb_{19+x}$ phases formed at 700°C.

At variance to $Ba_5V_{12}Sb_{19+x}$, a difference Fourier map of $Ba_5Nb_{12}Sb_{19+x}$ at z = 0.5 around Ba1 showed that the shape of electron density for Ba1 became less ellipsoidal (see Figure 4). Weak peaks appear at (½,½,½) (atom site Sb7 in $Ba_5V_{12}Sb_{19+x}$) and (0,0,0), which, however, disappeared after the Ba1 atom was added to the refinement. Although a split of this position into two atoms (Ba1a and Ba1b) resulted in a stable refinement without any constraints, the R-factor was not significantly reduced; therefore the Ba1 atom site was kept unsplit. In the final stage of refinement, a small residual electron density of ~5×10^3 e^-/nm^3 remained at (0,0,0) at 0.236 nm from the Sb4 atom. Attempts to assign this electron density to a partial occupancy of antimony or an oxygen atom resulted in unreliable and unstable ADP's. Therefore we conclude that this residual electron density most likely represents Fourier ripples.

The final formula $Ba_5Nb_{12}Sb_{19.14}$ derived from single crystal refinement, $Ba_{13.5}Nb_{33.5}Sb_{53.0}$ (in at. %), agrees very well with the phase composition measured by EPMA ($Ba_{13.8}Nb_{33.2}Sb_{53.0}$). Rietveld refinement for a nearly single-phase sample $Ba_5Nb_{12}Sb_{19+x}$ confirmed the structure model. Similar to its vanadium counterpart, the attempt to search for higher symmetry via PLATON did not reveal any missing symmetry. The Flack parameters are fairly close to zero (0.1) and do not suggest the presence of an inverted structure. Crystallographic data for $Ba_5Nb_{12}Sb_{19.14}$ are summarized in Table 3; interatomic distances are presented in Table 4. For a closer description of the crystal structure, see section below. Since we could not obtain a single crystal from equilibrium with the Sb-rich liquid, it is not clear whether the absence of Sb7 at (½,½,½) is related to a homogeneity range of $Ba_5Nb_{12}Sb_{19+x}$. However, the absence of an electron density at (½,½,½) resembles the structure of $Ba_5Ti_{12}Sb_{19+x}$, for which single crystals were obtained under different conditions from the Sb rich part.

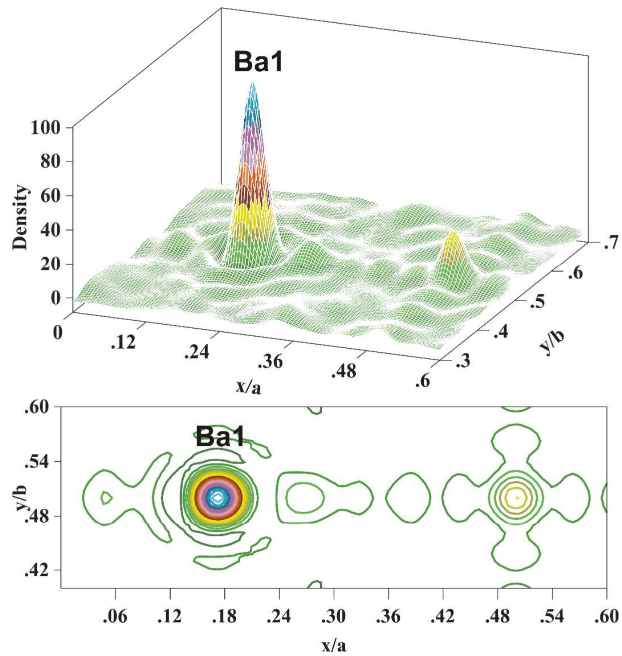

Figure 4. Difference Fourier map of $Ba_5Nb_{12}Sb_{19+x}$ at z = 0.5 around Ba1 from data measured at 100 K.

Table 1. Crystallographic data for $Ba_5V_{12}Sb_{19+x}$, x= 0.41; for comparison all atom labels and site parameters were kept consistent with the description of the parent crystal structure of $Ba_5Ti_{12}Sb_{19+x}$ (standardized).

Parameter/compound	**300 K**	**200 K**	**100 K**
Phase composition (EPMA, at.%)	$Ba_{13.3}V_{33.7}Sb_{53.0}$	$Ba_{13.3}V_{33.7}Sb_{53.0}$	$Ba_{13.3}V_{33.7}Sb_{53.0}$
Refinement composition (at.%)	$Ba_{13.4}V_{33.1}Sb_{53.5}$	$Ba_{13.4}V_{33.1}Sb_{53.5}$	$Ba_{13.4}V_{33.1}Sb_{53.5}$
Structure type	disordered-$Ba_5Ti_{12}Sb_{19+x}$	disordered-$Ba_5Ti_{12}Sb_{19+x}$	disordered-$Ba_5Ti_{12}Sb_{19+x}$
θ range (deg)	$4.75\leq2\theta\leq72.61$	$4.76\leq2\theta\leq72.53$	$4.76\leq2\theta\leq72.62$
a=*b*=*c* [nm] (from Kappa CCD)	1.21230(1)	1.21039(1)	1.20914(1)
a [nm] (from Guinier, Si-standard)	1.21391(5)	-	-
Reflections in refinement	1673 ≥ 4σ(F_o) of 1675	1670 ≥ 4σ(F_o) of 1671	1670 ≥ 4σ(F_o) of 1671
Number of variables	50	50	50
$R_{F2} = \Sigma\|F_o^2-F_c^2\|/\Sigma F_o^2$	0.0189	0.0181	0.0184
wR2	0.0421	0.0403	0.0420
R_{Int}	0.0380	0.0325	0.0326
GOF	1.295	1.350	1.392
Extinction (Zachariasen)	0.00040(1)	0.00034(2)	0.00029(1)
Ba1a in 6g (x,½,½); occ.	x = 0.1723(2); 0.46(1)	x = 0.1720(2); 0.46(1)	x = 0.1717(2); 0.46(1)
$U_{11};U_{22}=U_{33};U_{23};U_{13}=U_{12}=0$[1]	0.0644(5); 0.0121(2); -0.0015(2)	0.0586(5); 0.0078(2); -0.0011(2)	0.0514(5); 0.0035(2); -0.0008(2)
	$U_{equiv} = U_{iso} = 0.0115(4)$	$U_{equiv} = 0.0075(4)$	$U_{equiv} = 0.0036(4)$
Ba1b in 6g (x,½,½); occ.	x = 0.2028(2); 0.51(1)	x = 0.2022(2); 0.50(1)	x = 0.2014(2); 0.50(1)
$U_{11};U_{22}=U_{33};U_{23};U_{13}=U_{12}=0$[1]	$U_{equiv} = U_{iso} = 0.0143(4)$	$U_{equiv} = 0.0095(3)$	$U_{equiv} = 0.0045(3)$

Parameter/compound	300 K	200 K	100 K
Ba2 in 4e (x,x,x); occ. $U_{11}=U_{22}=U_{33};U_{23}=U_{13}=U_{12}$	x = 0.83405(4); 1.00(1) 0.0150(1); -0.0010(1)	x = 0.83401(3); 1.00 0.0100(1); -0.0008(1)	x = 0.83395(3); 1.00 0.0046(1); -0.0004(1)
V1 in 12i (x,x,z); occ. $U_{11}=U_{22};U_{33};U_{23}=U_{13};$ U_{12}	x = 0.1576(1); z = 0.3252(1); 1.00(1) 0.0074(2); 0.0094(4); 0.0009(2); 0.0003(3)	x = 0.1577(1); z = 0.3250(1); 1.00 0.0050(2); 0.0065(4); 0.0005(2); 0.0004(3)	x = 0.1578(1); z = 0.3249(1); 1.00 0.0025(2); 0.0034(4); 0.0004(2); 0.0004(3)
V2 in 12h (x,½,0); occ. $U_{11};U_{22};U_{33};$ $U_{23};U_{13}=U_{12}=0$	x = 0.1867(1); 1.00(1) 0.0059(3); 0.0063(3); 0.074(3); 0.0012(3)	x = 0.1869(1); 1.00 0.0038(3); 0.0042(3); 0.048(3); 0.0009(3)	x = 0.1870(1); 1.00 0.0014(3); 0.0018(3); 0.023(3); 0.0005(3)
Sb1 in 12i (x,x,z); occ. $U_{11}=U_{22};U_{33};U_{23}=U_{13};$ U_{12}	x = 0.21683(2); z = 0.54221(3); 1.00(1) 0.0087(1); 0.0104(1); -0.0011(1); -0.0011(1)	x = 0.21697(2); z = 0.54215(3); 1.00(1) 0.0057(1); 0.0069(1); -0.0008(1); -0.0008(1)	x = 0.21712(2); z = 0.54205(3); 1.00(1) 0.0025(1); 0.0030(1); -0.0005(1); -0.0004(1)
Sb2 in 12i (x,x,z); occ. $U_{11}=U_{22};U_{33};U_{23}=U_{13};$ U_{12}	x = 0.33272(2); z = 0.01344(3); 1.00(1) 0.0071(1); 0.0093(2); 0.0018(1); 0.0021(1)	x = 0.33265(2); z = 0.01325(3); 1.00 0.0047(1); 0.0062(1); 0.0013(1); 0.0014(1)	x = 0.33259(2); z = 0.01306(3); 1.00 0.0020(1); 0.0030(1); 0.0008(1); 0.0009(1)
Sb3 in 6f (x,0,0); occ. $U_{11};U_{22}=U_{33};U_{23};U_{13}=U_{12}=0$	x = 0.36550(4); 1.00 0.0056(2); 0.0060(1); -0.0011(2)	x = 0.36558(4); 1.00 0.0036(2); 0.0038(1); -0.0008(1)	x = 0.36562(4); 1.00 0.0011(2); 0.0015(1); -0.0006(2)
Sb4 in 4e (x,x,x); occ. $U_{11}=U_{22}=U_{33};U_{23}=U_{13}=U_{12}$	x = 0.11037(3); 1.00(1) 0.0095(1); -0.0004(1)	x = 0.11008(3); 1.00 0.0063(1); -0.0001(1)	x = 0.10977(3); 1.00 0.0028(1); -0.0001(1)
Sb5 in 4e (x,x,x); occ. $U_{11}=U_{22}=U_{33};U_{23}=U_{13}=U_{12}$	x = 0.31626(3); 1.00(1) 0.0082(1); 0.0005(1);	x = 0.31647(3); 1.00 0.0055(1); 0.0006(1);	x = 0.31671(3); 1.00 0.0027(1); 0.0008(1);
Sb6 in 4e (x,x,x); occ. $U_{11}=U_{22}=U_{33};U_{23}=U_{13}=U_{12}$	x = 0.460(1); 0.073(5) 0.025(4); -0.003(3);	x = 0.458(1); 0.075(5) 0.017(3); -0.002(2);	x = 0.4568(4); 0.079(4) 0.007(2); -0.002(2);
Sb7 in 1b (½,½,½); occ. $U_{11}=U_{22}=U_{33};U_{23}=U_{13}=U_{12}=0$	0.53(1) 0.030(2)	0.52(1) 0.020(1)	0.49(1) 0.011(1)
Residual electron density; max; min in (electron/nm^3) × 10^3	3.83;-1.57	4.00;-1.41	3.95;-1.33
Flack parameter	0.02(6)	0.01(6)	0.01(6)

[1]Independent refinement was also performed for unsplit Ba1 with anisotropic ADPs to extract Uij for analysis in Figure 8.

3.2. Structural chemistry of the phases $Ba_5\{V,Nb\}_{12}Sb_{19+x}$

Following the first structure description of $Ba_5Ti_{12}Sb_{19+x}$ by Bie and Mar,[3] the crystal structures of $Ba_5\{V,Nb\}_{12}Sb_{19+x}$ especially the Ba_5Sb_{19+x} substructure can be described in terms of the γ-brass structure (see Figure 5) as a consecutive nesting of polyhedra: an inner tetrahedron, surrounded by an outer tetrahedron, included by an octahedron, finally enclosed by a distorted cuboctahedron. The distortion in the cuboctahedron is due to rectangular faces instead of squares.

There are two types of such polyhedra per unit cell, one located at the corner of the unit cell and one in the center of unit cell. For the corner of unit cell, the inner tetrahedron, outer tetrahedron, octahedron, and the distorted cuboctahedron are formed by Sb4, Ba2, Sb3, and Sb2, respectively, while the nested polyhedra at the centre of the unit cell are formed by Sb6, Sb5, Ba1, and Sb1, respectively. Note that the cuboctahedron in the centre of unit cell is more distorted due to the larger difference between the two Sb1-Sb1 distances forming the cuboctahedron (0.41534 and 0.57207 nm). For $Ba_5V_{12}Sb_{19+x}$ atom site Sb7 resides inside the innermost tetrahedron at the centre of the unit cell.

Alternatively, the structure can be described as a combination of tetrahedrally arranged distorted icosahedra formed by Ba2[Sb_{12}] and nearly planar group-V metal nets. The metal nets are sandwiched between trigonal antiprisms (distorted octahedra) formed by Sb4[Ba_3V_3] and distorted heptahedra formed by Sb5[$Ba_3V_3Sb_4$] along the body diagonal (see Figure 6).

There are three main differences between the crystal structure of $Ba_5\{V,Nb\}_{12}Sb_{19+x}$ and the parent compound $Ba_5Ti_{12}Sb_{19+x}$: (i) the disorder in site Ba1 (in case of $Ba_5V_{12}Sb_{19+x}$), (ii) the partial filling of Sb7 in site 1b (in case of $Ba_5V_{12}Sb_{19+x}$), and (iii) the extremely short distances between Sb6 atoms. The disorder in the Ba1 site seems to be inferred by the nature of the group-V elements forming this compound, since the same feature was not encountered in $Ba_5Ti_{12}Sb_{19+x}$. This disorder could also be related to point (iii) where the partial filling of ~7.5% of Sb6 results in extremely short distances among Sb6 atoms. This holds true for $Ba_5V_{12}Sb_{19+x}$, where the site 1b is also partially filled by Sb7 atoms. Note, that in case of $Ba_5Nb_{12}Sb_{19+x}$, despite the electron density around Ba1 is rather spherical, the displacement parameter Ba1-U_{11} in direction towards Sb6 is still twice as big as for Ba1-$U_{22,33}$. The same partial filling of this site was also observed in $Ba_5Ti_{12}Sb_{19+x}$, however, in that case the position of Sb6 is much further away from the centre of the unit cell and therefore the distance between Sb6 atoms is not so short (dSb6-Sb6= 0.4757 nm).

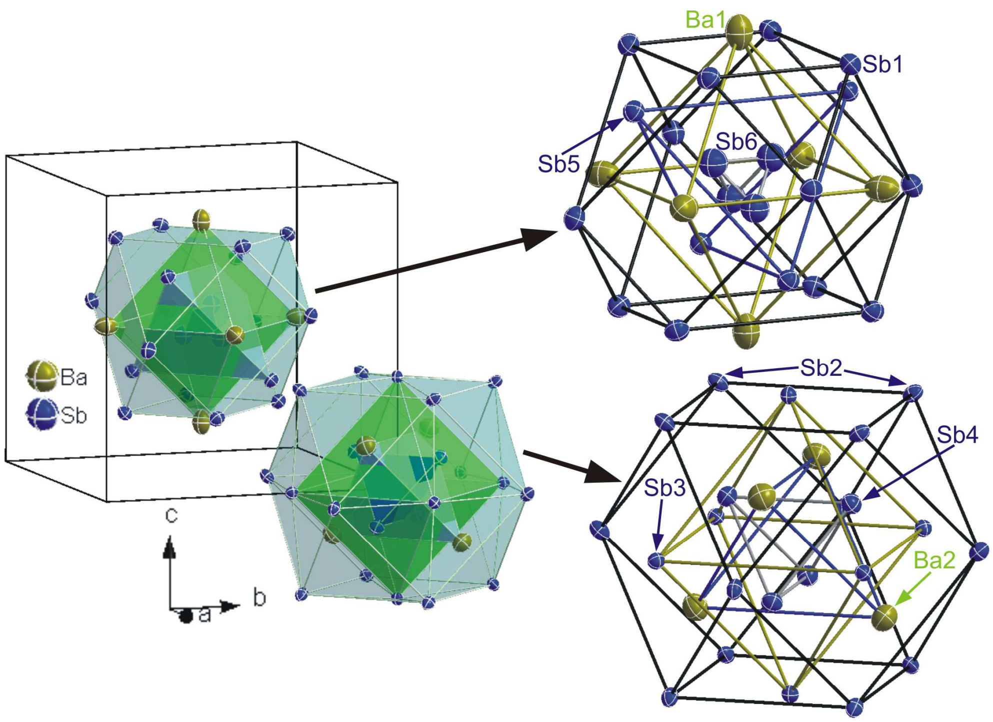

Figure 5. γ-brass cluster representation of $Ba_5\{Nb,V\}_{12}Sb_{19+x}$ with ADPs from SC refinement for $Ba_5Nb_{12}Sb_{19+x}$ at RT.

Table 2. Interatomic distances d in [nm] for $Ba_5V_{12}Sb_{19+x}$ (x=0.41). The coordination number, CN, is given for unsplit Ba1.

Atom 1	Atom 2	d [nm]	Atom 1	Atom 2	d [nm]	Atom 1	Atom 2	d [nm]
Ba1a	Sb2 (2x)	0.34542	V2	Sb2 (2x)	0.26969	Sb3	V1 (2x)	0.27451
CN=13	Sb1 (4x)	0.35126	CN=8	Sb1 (2x)	0.27028	CN=11	V2 (4x)	0.27894
	Sb6 (2x)	0.35511		Sb3 (2x)	0.27894		Sb3 (1x)	0.32612
	Sb5 (2x)	0.36016		V1 (2x)	0.28751		Sb4 (2x)	0.36258
	Sb2 (2x)	0.36459	Sb1	V2 (2x)	0.27028		Ba2 (2x)	0.37346
Ba1b	Sb6 (2x)	0.31882	CN=9	V1 (1x)	0.28209	Sb4	V1 (3x)	0.27265
CN=13	Sb5 (2x)	0.34372		Sb5 (1x)	0.32263	CN=6	Ba2 (3x)	0.34828
	Sb1 (4x)	0.34749		Sb2 (2x)	0.34736	Sb5	V1(3x)	0.27231
	Sb7(1x)	0.36024		Ba1b (2x)	0.34749	CN=10	Sb6 (1x)	0.30083
	Sb2 (2x)	0.36739		Ba1a (2x)	0.35126		Sb1(3x)	0.32263
	Sb2 (2x)	0.38859		Ba2 (1x)	0.36439		Ba1b (3x)	0.34372
Ba2	Sb4 (3x)	0.34828	Sb2	V2 (2x)	0.26969		Ba1a(3x)	0.36016
CN=12	Sb2 (3x)	0.35923	CN=9	V1 (2x)	0.27514	Sb6	Sb7 (1x)	0.08499
	Sb1 (3x)	0.36439		Ba1a (1x)	0.34542	CN=4[1]	Sb6 (3x)	0.13878
	Sb3(3x)	0.37346		Sb1 (2x)	0.34736		Sb5 (1x)	0.30083
V1	Sb5(1x)	0.27231		Ba2 (1x)	0.35923		Ba1b (3x)	0.31882
CN=10	Sb4 (1x)	0.27265		Ba1a (1x)	0.36459		Ba1a (3x)	0.35511
	Sb3 (1x)	0.27451		Ba1b (1x)	0.36739	Sb7	Sb6(4x)	0.08499
	Sb2 (2x)	0.27514		Sb5 (1x)	0.36819	CN=6[1]	Ba1b (6x)	0.36024
	Sb1(1x)	0.28209		Sb1 (2x)	0.38083		Sb5 (4x)	0.38582
	V1 (2x)	0.28733		Ba1b (1x)	0.38859		Ba1a (6x)	0.39733
	V2 (2x)	0.28751						

[1]Sb6 and Sb7 are excluded from the coordination polyhedra due to their short distance and small occupancy of Sb6, while Sb5 is located outside the polyhedra if unsplit Ba1 is considered.

Table 3. Crystallographic data for $Ba_5Nb_{12}Sb_{19+x}$, x= 0. 14; for comparison all atom labels and site parameters were kept consistent with the description of the parent crystal structure of $Ba_5Ti_{12}Sb_{19+x}$ (standardized).

Parameter/compound	300 K	200 K	100 K
Phase composition (EPMA, at.%)	$Ba_{13.5}Nb_{33.5}Sb_{53.0}$	$Ba_{13.5}Nb_{33.5}Sb_{53.0}$	$Ba_{13.5}Nb_{33.5}Sb_{53.0}$
Refinement composition (at.%)	$Ba_{13.8}Nb_{33.2}Sb_{53.0}$	$Ba_{13.8}Nb_{33.2}Sb_{53.0}$	$Ba_{13.8}Nb_{33.2}Sb_{53.0}$
Structure type	$Ba_5Ti_{12}Sb_{19+x}$	$Ba_5Ti_{12}Sb_{19+x}$	$Ba_5Ti_{12}Sb_{19+x}$
θ range (deg)	$2\leq 2\theta \leq 72.55$	$2\leq 2\theta \leq 72.55$	$2\leq 2\theta \leq 72.45$
$a=b=c$ [nm] (from Kappa CCD)	1.24979(2)	1.24827(2)	1.24691(2)
a[nm] (from Guinier, Si-standard)	1.2501(3)	-	-
Reflections in refinement	$1623 \geq 4\sigma(F_o)$ of 1758	$1701 \geq 4\sigma(F_o)$ of 1787	$1721 \geq 4\sigma(F_o)$ of 1786
Number of variables	46	46	46
$R_{F2} = \Sigma\|F_o^2-F_c^2\|/\Sigma F_o^2$	0.0219	0.0202	0.0184
wR2	0.0449	0.0401	0.0355
R_{Int}	0.0176	0.0149	0.0143
GOF	1.137	1.121	1.118
Extinction (Zachariasen)	0.00021(1)	0.00020(1)	0.00018(1)
Ba1 in 6g (x,½,½); occ.	x = 0.17161(5); 1.00(1)	x = 0.17138(4); 1.00(1)	x = 0.17111(4); 1.00(1)
U_{11};U_{22}=U_{33};U_{23};U_{13}=U_{12}=0	0.0311(3); 0.0181(1); 0.0003(2)	0.0235(2); 0.0127(1); 0.0003(2)	0.0159(2); 0.0072(1); -0.0001(2)
Ba2 in 4e (x,x,x); occ.	x = 0.83454(4); 1.00(1)	x = 0.83456(3); 1.00(1)	x = 0.83457(3); 1.00(1)
U_{11}=U_{22}=U_{33};U_{23}=U_{13}=U_{12}	0.0213(1); -0.0021(1)	0.0151(1); -0.0015(1)	0.0086(1); -0.0009(1)
Nb1 in 12i (x,x,z); occ.	x = 0.16023(3); z = 0.32652(4); 1.00(1)	x = 0.16022(2); z = 0.32641(4); 1.00(1)	x = 0.16017(2); z = 0.32633(4); 1.00(1)
U_{11}=U_{22};U_{33};U_{23}=U_{13}; U_{12}	0.0089(1); 0.0091(2); 0.0015(2); 0.001(2)	0.0066(1); 0.0069(2); 0.0010(1); 0.007(1)	0.0042(1); 0.0044(2); 0.0005(1); 0.0004(1)
Nb2 in 12h (x,½,0); occ.	x = 0.18670(4); 1.00(1)	x = 0.18686(3); 1.00(1)	x = 0.18699(3); 1.00(1)
U_{11};U_{22};U_{33}; U_{23};U_{13}=U_{12}=0	0.0087(2); 0.0080(2); 0.0094(2); 0.0016(2)	0.0066(2); 0.0060(2); 0.0070(2); 0.0009(2)	0.0041(2); 0.0039(2); 0.0042(2); 0.0005(2)
Sb1 in 12i (x,x,z); occ.	x = 0.22067(2); z = 0.54434(3); 1.00(1)	x = 0.22079(2); z = 0.54429(3); 1.00(1)	x = 0.22093(2); z = 0.54423(2); 1.00(1)
U_{11}=U_{22};U_{33};U_{23}=U_{13}; U_{12}	0.0117(1); 0.0141(2); -0.0014(1); -0.0007(1);	0.0084(1); 0.0102(1); -0.0010(1); -0.0005(1);	0.0049(1); 0.0061(1); -0.0005(1); -0.0002(1);
Sb2 in 12i (x,x,z); occ.	x = 0.33233(2); z = 0.00887(3); 1.00(1)	x = 0.33226(2); z = 0.00868(3); 1.00(1)	x = 0.33221(2); z = 0.00849(3); 1.00(1)
U_{11}=U_{22};U_{33};U_{23}=U_{13}; U_{12}	0.0096(1); 0.0111(2); 0.0022(1); 0.0022(1)	0.0070(1); 0.0081(1); 0.0014(1); 0.0016(1)	0.0042(1); 0.0048(1); 0.0008(1); 0.0009(1)
Sb3 in 6f (x,0,0); occ.	x = 0.36280(4); 1.00(1)	x = 0.36293(4); 1.00(1)	x = 0.36302(4); 1.00(1)
U_{11};U_{22}=U_{33};U_{23};U_{13}=U_{12}=0	0.0089(2); 0.0082(1); -0.0005(2)	0.0068(2); 0.0059(1); -0.0005(2)	0.0043(2); 0.0036(1); -0.0002(2)
Sb4 in 4e (x,x,x); occ.	x = 0.10884(3); 1.00(1)	x = 0.10853(3); 1.00(1)	x = 0.10829(3); 1.00(1)
U_{11}=U_{22}=U_{33};U_{23}=U_{13}=U_{12}	0.0122(1); -0.0008(1);	0.0089(1); -0.0004(1);	0.0054(1); -0.0001(1);
Sb5 in 4e (x,x,x); occ.	x = 0.32277(3); 1.00(1)	x = 0.32283(3); 1.00(1)	x = 0.32290(3); 1.00(1)
U_{11}=U_{22}=U_{33};U_{23}=U_{13}=U_{12}	0.0115(1); -0.0005(1);	0.0083(1); -0.0002(1);	0.0049(1); 0.0001(1);
Sb6 in 4e (x,x,x); occ.	x = 0.4521(6); 0.067(4)	x = 0.4515(4); 0.077(3)	x = 0.4515(4); 0.074(3)
U_{11}=U_{22}=U_{33};U_{23}=U_{13}=U_{12}	U_{iso}= 0.020(3)	U_{iso}= 0.016(2)	U_{iso}= 0.008(2)
Residual electron density; max; min in (electron/nm^3) × 10^3	5.02;-2.26	5.65;-1.82	5.35;-1.32
Flack parameter	0.10(3)	0.10(2)	0.24(2)

Table 4. Interatomic distances d in [nm] for $Ba_5Nb_{12}Sb_{19+x}$.

Atom 1	Atom 2	d [nm]	Atom 1	Atom 2	d [nm]	Atom 1	Atom 2	d [nm]
Ba1	Sb1 (4x)	0.35875	Nb2	Sb2 (2x)	0.27778	Sb3	Nb1 (2x)	0.28681
CN=12	Sb2 (2x)	0.35943	CN=10	Sb1 (2x)	0.28449	CN=11	Nb2 (4x)	0.28956
	Sb6 (2x)	0.36059		Sb3 (2x)	0.28956		Sb3 (1x)	0.34295
	Sb5 (2x)	0.36581		Nb1 (2x)	0.29699		Sb4 (2x)	0.37114
	Sb2 (2x)	0.37243		Nb2 (2x)	0.32998		Ba2 (2x)	0.38256
Ba2	Sb4 (3x)	0.35713	Sb1	Nb2 (2x)	0.28449	Sb4	Nb1 (3x)	0.28682

CN=12	Sb2 (3x)	0.36668	CN=9	Nb1 (1x)	0.29243	CN=6	Ba2 (3x)	0.35713
	Sb1 (3x)	0.37558		Sb5 (1x)	0.33052	Sb5	Sb6 (1x)	0.27984
	Sb3 (3x)	0.38256		Sb2 (2x)	0.35431	CN=10	Nb1 (3x)	0.28732
Nb1	Sb2 (2x)	0.28653		Ba1 (2x)	0.35875		Sb1 (3x)	0.33052
CN=10	Sb3 (1x)	0.28681		Ba2 (1x)	0.37558		Ba1 (3x)	0.36581
	Sb4 (1x)	0.28682	Sb2	Nb2 (2x)	0.27778	Sb6	Sb6 (3x)	0.16953
	Sb5 (1x)	0.28732	CN=9	Nb1 (2x)	0.28653	CN=4[1]	Sb5 (1x)	0.27984
	Sb1 (1x)	0.29243		Sb1 (2x)	0.35431		Ba1 (3x)	0.36059
	Nb1 (2x)	0.29392		Ba1 (1x)	0.35943			
	Nb2 (2x)	0.29699		Ba2 (1x)	0.36668			
				Ba1 (1x)	0.37243			

[1]Sb6 is excluded from the coordination polyhedra due to its short distance and small occupancy.

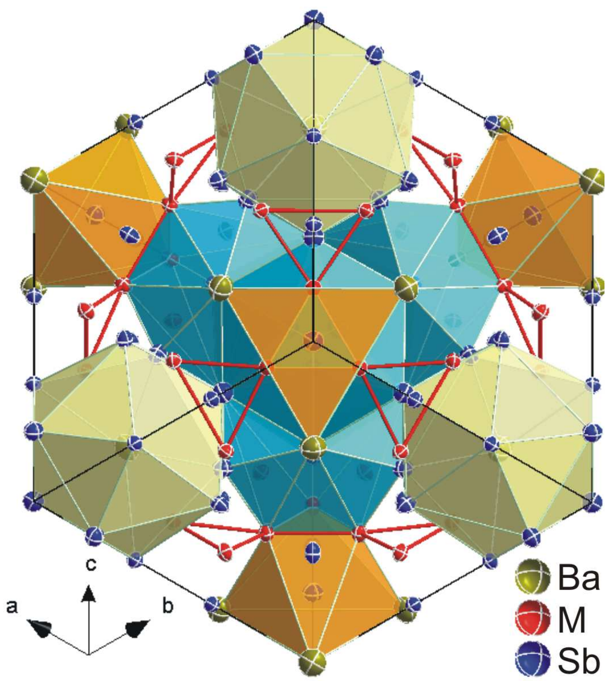

Figure 6. Projection of $Ba_5M_{12}Sb_{19+x}$ along <111> direction.

The short distance between Sb6 atoms in $Ba_5\{V,Nb\}_{12}Sb_{19+x}$ implies that this site cannot be fully occupied. This was confirmed by DFT calculations for $Ba_5Ti_{12}Sb_{19+x}$ where a full occupancy of Sb6 creates a rather short Sb1-Sb6 bonding distance of 2.8 Å and thereby reduces the Ti-Ti and Ti-Sb bonding stability.[3]

As mentioned in the previous section, the presence of Sb7 in site 1b (½,½,½) seems to increase the degree of disorder in the Ba1 site. However, since the Sb7 position is located just ~0.085 nm from the Sb6 position, both sites cannot be simultaneously filled. Reassuringly both sites are not capable of maintaining full occupancy, i.e. Sb6 and Sb7 sites show 7.5% and 50% occupancy.

Bond distance analyses for Ba1 split positions and partially occupied sites Sb6 and Sb7 (see Figure 7) revealed little correspondence with the occupancy, since both Ba1 split positions have similar occupancy. The distance between Ba1b (occupancy = 51%) and Sb7 corresponds much better to the sum of atomic radii [25] than the distance between Ba1a (occupancy = 46%) and Sb7. While the distance between Ba1b and Sb6 (0.30347 nm) is too short for a Ba-Sb contact, the distance between Ba1a and Sb6 shows good correspondence with the sum of atomic radii. Nevertheless, the higher occupancy of Ba1b corresponds to the Sb site with the higher occupancy (Sb7).

Similarly short Ba-Sb distances (<0.32 nm) can only be found in $BaSb_2F_{12}$ ($d_{Ba\text{-}Sb}$=0.2951 nm).[2] The combination of electropositive elements such as Ba and highly electronegative F (electronegativity=3.98) may suggest a strong ionic character of Ba, thus reducing the radii and consequently the interatomic distances.

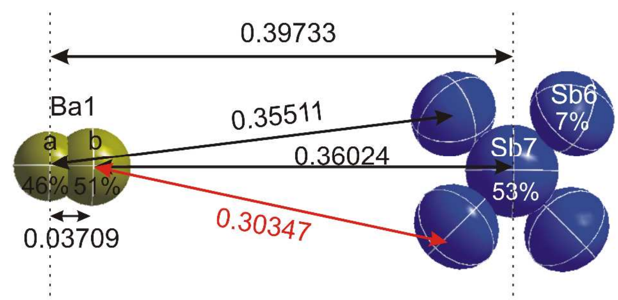

Figure 7. Bond distance (in nm) analysis between split Ba1, Sb6 and Sb7

It is interesting to note that a small vacancy level (~0.03) exists in $Ba_5V_{12}Sb_{19.41}$ for the Ba1 site. The vacancy is still present even when no splitting with anisotropic ADPs was applied. On the other hand, the Ba1 site in $Ba_5Nb_{12}Sb_{19.14}$ prefers to retain full occupancy even without anisotropic ADPs.

3.3. Physical properties

3.3.1. Lattice dynamics

Temperature dependent ADPs in $Ba_5V_{12}Sb_{19+x}$ (see Figure 8) for the framework atoms V and Sb (except Sb6 and Sb7) reveal a significantly smaller slope than for the Ba atoms. Treating the framework atoms as Debye oscillators according to Eqn. (1)

$$U_{eq} = \frac{3\hbar^2 T}{m k_B \theta_D^2}\left[\frac{T}{\theta_D}\int_0^{\theta_D/T}\frac{x}{e^x-1}dx+\frac{\theta_D}{4T}\right]+d^2 \quad (1)$$

where U_{eq} is calculated from the anisotropic thermal displacement parameters (U_{ii}), $U_{eq}= (U_{11}+U_{22}+U_{33})/3$, $\hbar$ is the reduced Planck's constant, k_B is the Boltzmann constant, m is the weighted average mass of the framework atoms (based on the site multiplicity), the Debye temperature θ_D can be extracted, together with the static disorder parameter d^2. Since the framework consists of two V and five Sb atoms, the value of U_{av} is taken from the weighted average of U_{eq} of V and Sb atoms. The Debye temperature obtained from this fit is $\theta_{D,av} = 229$ K.

The two Ba atoms and Sb7 show large ADPs (rattling behaviour) and thus, can be treated as Einstein oscillators,

$$U_{ii} = \frac{\hbar^2}{2mk_B\theta_{Eii}}\coth\left(\frac{\theta_{Eii}}{2T}\right) + d^2 \quad (2)$$

where θ_{Eii} is the corresponding Einstein temperature to the U_{ii}.

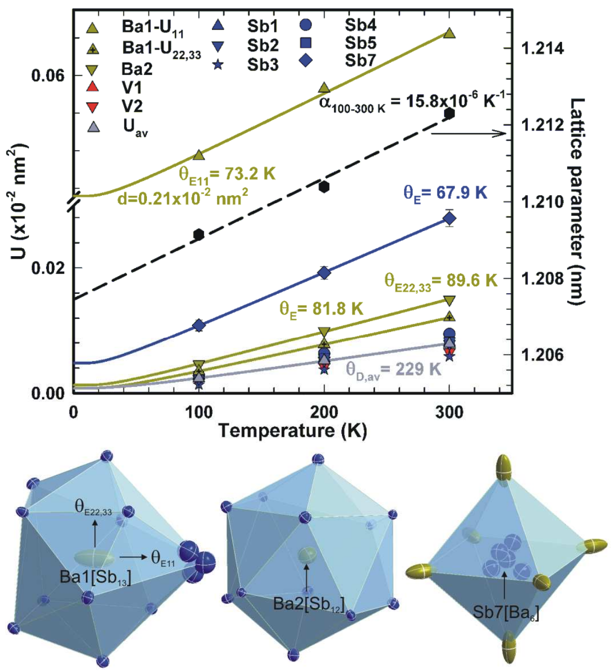

Figure 8. Upper panel: temperature dependent lattice parameters and ADPs (U_{eq}) for $Ba_5V_{12}Sb_{19.41}$. The solid lines represent the fit for the ADPs according to Eqn. (1) and (2), while the dashed line is the linear fit for the lattice parameters. Lower panel: atom coordination around atoms Ba1, Ba2 and Sb7 with ADPs from the SC refinement at RT.

Despite having similar behaviour as Sb7, atom Sb6 was not included in the calculation due to its small occupancy (less than 10%). Because of the site symmetry constraint $U_{11}=U_{22}=U_{33}$ for Ba2 and Sb7, only one Einstein temperature of 81.8 K and 67.9 K could be extracted from the fitting process, respectively. However, for unsplit Ba1, two Einstein temperatures, θ_{E11}= 73.2 K and $\theta_{E22,33}$= 89.6 K were determined. The disorder at the Ba1 site, caused by the presence of the Sb7 atom, can be clearly seen from the ellipsoid's direction towards Sb7, which corresponds to θ_{E11} (see Figure 8). The separation distance between the split Ba1 atoms (0.0371 nm) corresponds very well with the disorder parameter ($d^2=0.21\times10^{-2}$ nm^2) obtained from the fitting process.

Similar to $Ba_5V_{12}Sb_{19.41}$, Nb and Sb atoms (except Sb6) form the framework structure in $Ba_5Nb_{12}Sb_{19.14}$ (see Figure 9). The corresponding Debye temperature obtained from a fit to equation (1) is θ_D=206 K, which is somewhat lower than that of $Ba_5V_{12}Sb_{19.4}$. Such a trend is in good agreement with the simple vibrational spring approximation, in which the Debye temperature (frequency) is inversely proportional to the square root of atom mass. Since Sb7 is not present, Ba atoms are the only remaining rattlers in $Ba_5Nb_{12}Sb_{19.14}$. The Einstein temperatures related to these two atom sites are θ_{E11}= 66.3 K and $\theta_{E22,33}$=78.3 K for Ba1 and θ_E=72.5 K for Ba2.

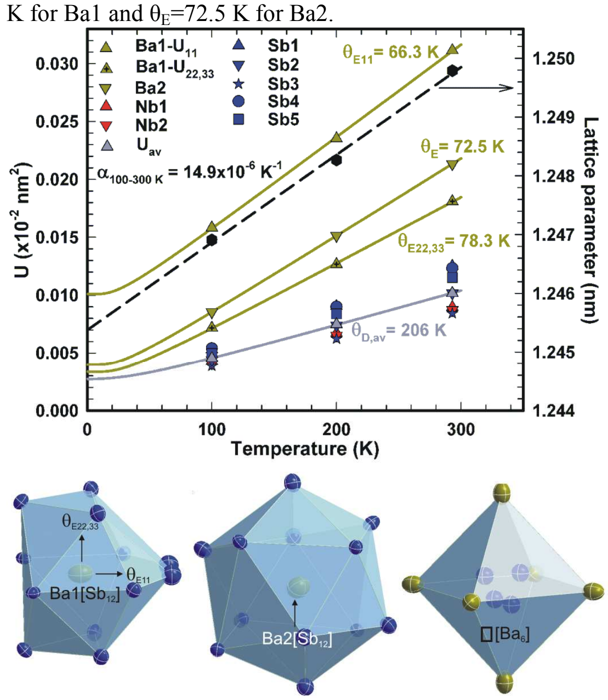

Figure 9. Upper panel: temperature dependent lattice parameters and ADPs (U_{eq}) for $Ba_5Nb_{12}Sb_{19.14}$. The solid lines represent the fit for the ADPs according to Eqn. (1) and (2), while the dashed line is the linear fit for the lattice parameters. Lower panel: atom coordination around atoms Ba1, Ba2 and Sb7 with ADPs from the SC refinement at RT. The open square symbol represents the vacancy in the 1b site.

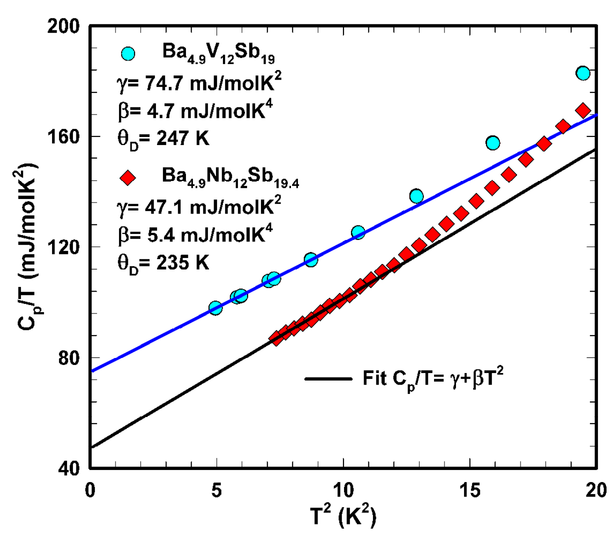

Figure 10 Low temperature specific heat Cp/T vs. T² of polycrystalline $Ba_5\{V,Nb\}_{12}Sb_{19+x}$ (composition from EPMA).

To get additional information on the lattice dynamics of $Ba_5\{V,Nb\}_{12}Sb_{19+x}$, heat capacity measurements were carried out. For non magnetic materials the specific heat (C_p) can be described as the sum of the electronic (C_{el}) and the lattice (C_{lat}) contribution. The electronic contribution at low temperatures varies linearly with temperature according to the Sommerfeld approximation, whilst at sufficiently low temperature ($T \ll \theta_D$) the lattice part can be approximated with the Debye T^3 law, i.e.,

$$C_p = C_{el} + C_{lat} = \gamma T + \beta T^3;\ \beta = \frac{12R\pi^4 n}{5\theta_D^{\,3}} \quad . \quad (3)$$

Here, γ and β are the coefficients of the electron and the lattice contribution, respectively, R is the gas constant and n is number of atoms in the formula unit.

The analysis of the low temperature specific heat of polycrystalline $Ba_{4.9}V_{12}Sb_{19.0}$ (presented in Figure 10) according to Eqn. 3 yields a Sommerfeld coefficient, γ = 74.7 mJ/molK^2, (2.08 mJ/g-at.K^2) which refers to a large value of the electronic density of states at the Fermi energy ($N(E_F)$). The Debye temperature, θ_D=247 K, extracted via Eqn. (3) is in good agreement with the value obtained from the ADPs (229 K). The specific heat data of $Ba_{4.9}Nb_{12}Sb_{19.4}$, on the other hand, show a lower Sommerfeld coefficient of γ = 47.1 mJ/molK^2 (1.29 mJ/g-at.K^2), which indicates a metallic state with a smaller electronic density of states at the Fermi energy as compared to $Ba_{4.9}V_{12}Sb_{19.0}$.

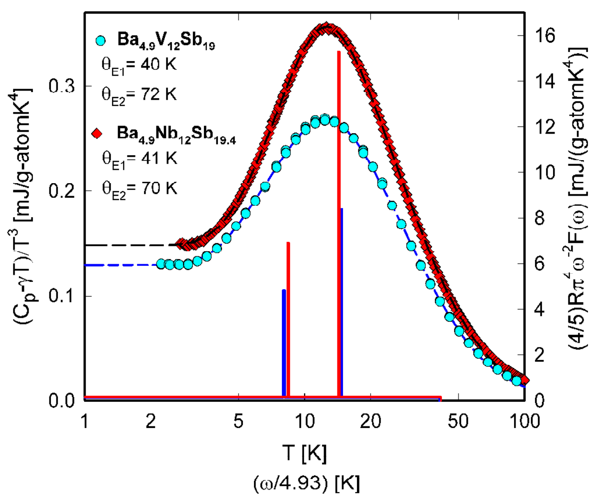

Figure 11 Junod fit (dashed lines) for the lattice contribution to the specific heat and the phonon density of states (solid lines) displayed as $F(\omega)/\omega^2$ of $Ba_5\{V,Nb\}_{12}Sb_{19+x}$ (composition from EPMA).

The obvious deviations of the experimental specific heat data of both compounds in Figure 10 from the simple Debye approximation of Eqn. 3 starting already above about 10 K^2 are indicative for the presence of Einstein modes with rather low energies. Accordingly, we perform a more detailed analysis of the lattice contribution to the specific heat via a so-called Junod fit [26] (Figure 11) providing a reasonable parameterization of the experimental data for both compounds with two narrow Einstein modes, $\theta_{E1} \sim 40$ K and $\theta_{E2} \sim 70$ K with similar width of ~1 K. The value of θ_{E2} is very close to the values of $\theta_{E,Sb7}$ and $\theta_{E,Ba(1,2)}$ obtained from the analysis of the ADPs. Note that the chemical formula of the vanadium compound derived from EPMA ($Ba_{4.9}V_{12}Sb_{19.0}$) does not show any extra antimony either as Sb6 or Sb7, however, since the contributions of those sites to the overall composition are small, they may fall within the error of the EPMA measurement (±0.5 at. %).

From the practically linear temperature dependent lattice parameters, coefficients of thermal expansion, $\alpha = 14.9\times10^{-6}$ K^{-1} and 15.8×10^{-6} K^{-1}, were obtained from the fit between 100-300 K for $Ba_5Nb_{12}Sb_{19+x}$ and $Ba_5V_{12}Sb_{19+x}$, respectively. Such large values of α exceed the maximum value reported for p-type Sb-based skutterudites,[12] but lie in range of some type-I clathrates.[27]

The previously derived Debye temperatures can be used to approximate the speed of sound

$$\upsilon_s = \frac{\theta_D k_B}{\hbar}\sqrt[3]{6\pi^2\frac{n}{V}} \quad , (4)$$

where n is the number of atom in the unit cell and V is the unit cell volume.

The resulting values of ~2235 and ~2076 m/s for $Ba_5V_{12}Sb_{19+x}$ and $Ba_5Nb_{12}Sb_{19+x}$, respectively, are lower than those of filled skutterudites, [12] suggesting a lower lattice thermal conductivity, λ_{ph},

$$\lambda_{ph} = \frac{1}{3}\upsilon_s \ell_{ph} C_v \quad , (5)$$

where ℓ_{ph} is the phonon mean free path and C_v is the specific heat at constant volume. The phonon mean free path can be estimated from the distance between rattler atoms.[28] By neglecting Sb7 atoms, the average distance between Ba atoms in $Ba_5\{Nb,V\}_{12}Sb_{19+x}$ is <0.6 nm; this is lower than the distance between filler atoms in Sb based skutterudites (>0.7 nm) [2]. Using the values mentioned above, together with the measured specific heat of $Ba_5V_{12}Sb_{19+x}$ at 300 K (~800 J/molK), the estimated lattice thermal conductivity is in the order of ~1 Wm^{-1}K^{-1}.

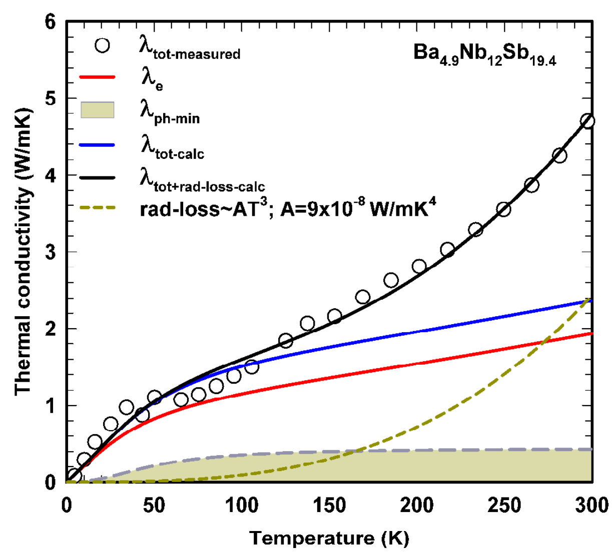

Figure 12. Temperature dependent thermal conductivity of $Ba_{4.9}Nb_{12}Sb_{19.4}$. The solid and the dashed lines are model curves as explained in the text.

Measurements of the thermal conductivity of $Ba_{4.9}Nb_{12}Sb_{19.4}$ seem to confirm the prediction mentioned above, due to its glass-like behaviour, and the low measured value near room temperature (~5 W/m.K, see Figure 12). As expected from the presence of defects and disorder, the frequently obeserved maximum of λ_{ph} (as typical for almost defect free materials) at low temperatures is suppressed. Attempts to extract and analyze the lattice contribution to the overall thermal conductivity in terms of Callaway's model [29–31] did not result in reliable outcomes. This is likely due to the dominant contribution of the electronic part to the overall thermal conductivity as a consequence of the relatively low electrical resistivity of this compound (see below). Indeed the electronic contribution calculated via the Wiedemann Franz law, using the Lorenz number (L_0) for a free electron system, $L_0 = 2.45\times10^{-8}$ WΩ/K^2 (see Figure 12), covers most of the overall measured thermal conductivity up to ~100 K. Assuming the minimum lattice thermal conductivity as proposed by Cahill and Pohl,[32] the difference between the measured data and the sum of the lattice and electronic thermal conductivity could be well approximated, together with radiation losses ~AT^3. At room temperature, the latter amounts to about ~2.5 W/mK, typically for the measurement set-up used in this study.

3.3.2. Electrical resistivity

Due to the brittleness of the $Ba_{4.9}V_{12}Sb_{19.0}$, the sample specimen (a cuboid of ~8x2x2 mm³) contained a significant amount of cracks, yielding a rather high resistivity at room temperature, ρ~40 μΩm. To reduce the influence of cracks, a smaller piece (~3 mm length) was used for electrical resistivity measurements with spot welded Au contacts, revealing a significantly lower room temperature resistivity (~18 μΩm). However, the absolute value of ρ of $Ba_{4.9}V_{12}Sb_{19.0}$ could not be measured with confidence, and thus ρ is presented as normalized electrical resistivity (ρ/ρ_{RT}). On the other hand, the $Ba_{4.9}Nb_{12}Sb_{19.4}$ sample shows better mechanical stability; therefore the absolute value of electrical resistivity could be reliably measured and analyzed.

Both compounds exhibit below room temperature a metallic-like temperature dependent electrical resistivity (Figure 13), reaching a minimum at ~10 K, followed by a slight increase of $\rho(T)$ towards lower temperatures. Above room temperature, $\rho(T)$ features a transition from a metallic to a more semiconducting behaviour. This holds true in case of $Ba_{4.9}Nb_{12}Sb_{19.4}$, while for $Ba_{4.9}V_{12}Sb_{19.0}$ the electrical resistivity seems to reach saturation near room temperature, presumably being the beginning of the transition towards a semiconducting behaviour.

In order to describe the temperature dependent electrical resistivity of both samples, various scattering mechanisms are considered, and additionally, a temperature dependent charge carrier density, n_{ch}, is introduced. The former can be accounted for in terms of independent relaxation times (τ_i), describing scattering of electrons by defects and impurities, by phonons and by other electrons. Quantitatively, for simple metallic systems, scattering on static imperfections is assumed to be temperature independent (residual resistivity ρ_0), while the electron phonon interaction is accounted for by a modified Bloch-Grüneisen model taking into account both acoustic and optical phonon scattering [33], i.e.,

$$\rho(T) = \rho_0 + \rho_{ph}(T), \qquad (6)$$

with

$$\rho_{ph} = \Re_A \left(\frac{T}{\theta_D}\right)^5 \int_0^{\frac{\theta_D}{T}} \frac{z^5}{(e^z-1)(1-e^{-z})}dz + \frac{\Re_O \theta_E^2}{T(e^x-1)(1-e^{-x})}; x = \frac{\theta_E}{T}, \qquad (7)$$

ρ_{ph} is the resistivity arising from electron-phonon scattering, $\Re_A$ and $\Re_O$ are the electron acoustic phonon and the electron optical phonon interaction constants, respectively. θ_D and θ_E are the Debye and the Einstein temperatures, respectively. Electron – electron scattering is omitted here; this term is of importance only at very low temperatures and/or in systems with strong correlations among electrons. Combing Eqn. 6 and 7 reveals a constant value for $T\rightarrow0$, a T^5 term at low and a linear temperature dependence at elevated temperatures. Obviously, both compounds (see Figure 13) do not follow that simple metallic scenario; rather the maximum and the drop of the resistivity at high temperatures as observed for the Ba-Nb-Sb system indicates some activated behaviour due to the presence of a gap in the electronic density of states near to the Fermi energy E_F. In order to describe such a scenario, we have developed a model using a box-like density of state with height *N(E),* where the valence and the conduction bands are separated by a gap with width E_g; the Fermi energy can be located either in the valence band, below the band edge (E_1) of this band, or in the conduction band, above the respective band edge (compare, inset, Fig. 13 (a)). This simple band structure allows to analytically deriving the charge carrier concentration of both holes, n_h, and electrons, n_e, with $n_{ch}(T) = \sqrt{n_e(T)n_h(T)} + n_{ch}^0$. Calculations have to be done employing the Fermi-Dirac distribution function. In addition, this model allows for in-gap states as well, as sketched in the inset of Figure 13 (a). Eqn. 6 then modifies to

$$\rho(T) = \frac{n_{ch}^0\left(\rho_0 + \rho_{ph}(T)\right)}{n_{ch}(T)} \qquad (8)$$

n_{ch}^0 is a residual charge carrier density (see ref. [34] and the supporting information for detailed descriptions).

Applying Eqns. 7 and 8 to the experimental data reveals excellent agreement (solid lines in Figure 13 (a,b)) for the whole temperature range studied. Relevant parameters describing our model are indicated in both figures. Since the measurement of $Ba_{4.9}V_{12}Sb_{19.0}$ is restricted to temperatures below 300 K, we started the fit procedure with the $Ba_{4.9}Nb_{12}Sb_{19.4}$ sample and used those fit parameters as starting values to account for $Ba_{4.9}V_{12}Sb_{19.0}$ as well. Reasonable values of the various material parameters are revealed, e.g., the narrow gaps in the electronic density of states.

The present band model provides a large variation of temperature dependencies of the electrical resistivity, without involving scattering processes others than electron – static impurity and electron – phonon interaction. The overall resistivity behaviour as observed experimentally is thus a balance of an increasing contribution due to electron scattering by phonons with respect to the temperature dependent variation of the charge carrier concentration. Subtle changes of the various parameters involved in this model can cause dramatic changes of ρ(T). Focusing e.g., on the negative slope of the resistivity at very low temperatures observed in both present compounds, does not require a description based on the Kondo effect or weak localisation due to disorder in the crystal; rather, a stronger increase of $n_{ch}(T)$ in relation to the initial increase of $\rho_{ph}(T)$ results in a low temperature decrease of the electrical resistivity as the temperature raises. In other words, thermodynamics outweighs standard scattering scenarios in systems, which are near to a metal-to-insulator transition.

The resistivity change from metal towards semiconducting behaviour in $Ba_{4.9}Nb_{12}Sb_{19.4}$ is in line with the occurrence of a maximum in the Seebeck coefficient vs temperature (see inset Figure 13a). A crossover from p- to n-type conductivity is also observed in $Ba_{4.9}Nb_{12}Sb_{19.4}$ at ~680 K, which is usually accompanied by a large value of electrical resistivity. However in this case the existence of a small energy gap (~50 meV) obtained from the resistivity fit could explain the low resistivity value of this compound. The small difference between the Fermi level and the valence band edge (~4 meV) together with the small energy gap may be responsible for the crossover from p- to n-type.

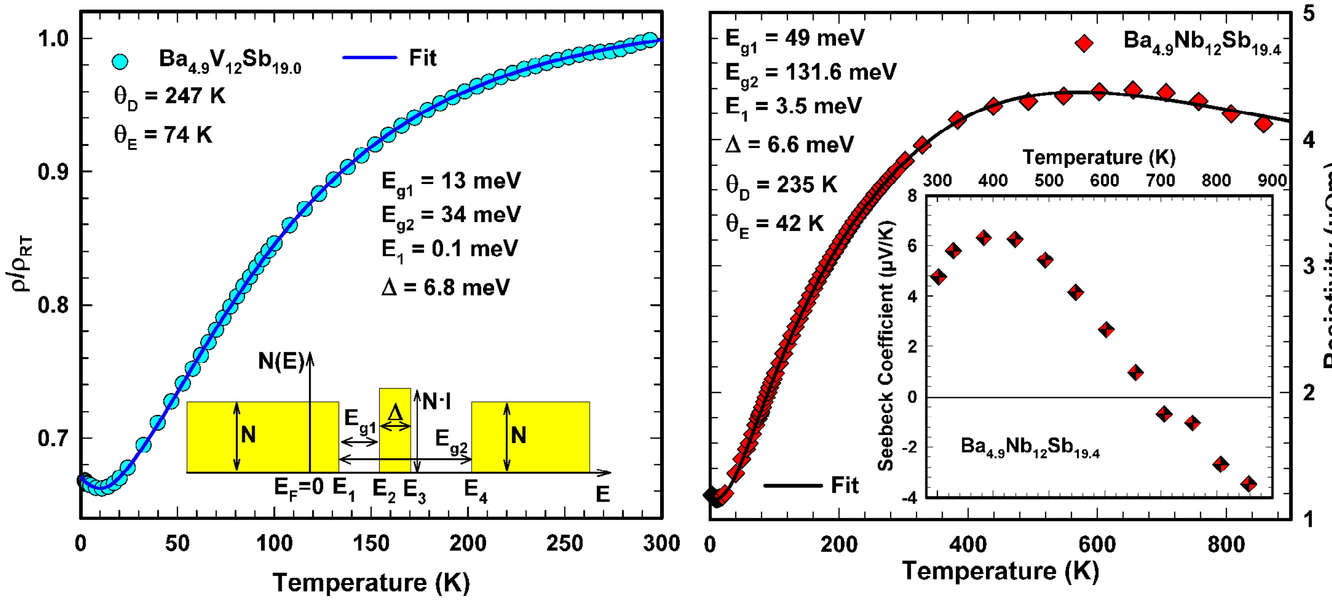

Figure 13. Temperature dependent electrical resistivity of $Ba_5(V,Nb)_{12}Sb_{19+x}$ and high temperature Seebeck coefficient of $Ba_{4.9}Nb_{12}Sb_{19.4}$. Solid lines represent the least squares fit according to Eqn. 7 and Eqn. 8.

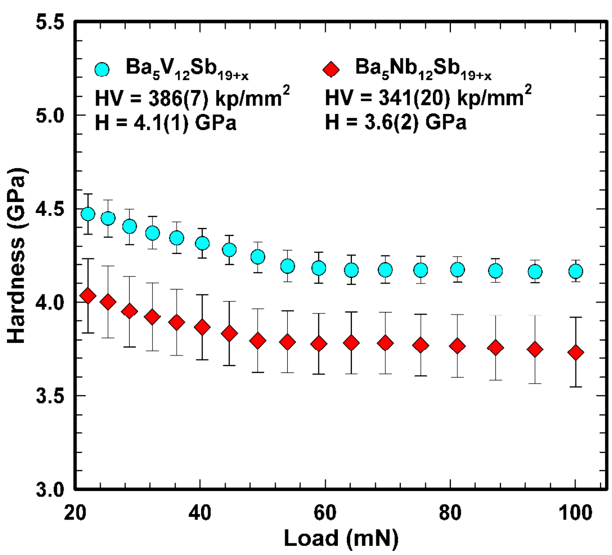

Figure 14. Load dependent hardness of $Ba_5(V,Nb)_{12}Sb_{19+x}$.

3.3.3. Mechanical properties

Hardness measurement on a polished surface of $Ba_{4.9}V_{12}Sb_{19.0}$ and $Ba_{4.9}Nb_{12}Sb_{19.4}$ employing a nano-indenter resulted in a hardness value of (4.1±0.1) GPa equivalent to HV = 386 kp/mm^2 and (3.6±0.2) GPa equivalent to HV = 341 kp/mm^2, respectively. Load dependent hardness measurements (see Figure 14) clearly show saturation yielding the true hardness value for loads of more than 50 mN. The hardness measured is in the range of filled Sb-based skutterudites,[12] which suggests a similar type of bonding.

An estimate for indentation Young's modulus (E_I) was derived from the nano-indentation experiment assuming a Poisson's ratio (ν) as for $V_{1-x}Sb_2$ (ν = 0.26).[15] This yields E_I=(85±2) GPa, a value much smaller than that for filled skutterudites. Details on the hardness and Young's modulus measurement via nanoindentation can be found in ref.[35] and from references therein.

For isotropic materials, the shear (G) and bulk (B) moduli can be calculated employing Eqn. 9 (see Table 5 for the results):

$$G = \frac{E}{2(\nu+1)} \quad \text{and} \quad B = \frac{E}{3(1-2\nu)} \qquad (9)$$

For isotropic materials the mean sound velocity estimated from Anderson's formulae[36] (Eqn. 10) could be used to calculate the Debye temperature:

$$\theta_D = \frac{h\upsilon_m}{k_B}\sqrt[3]{\frac{3nN_A D}{4M\pi}}; \quad \text{with} \quad \upsilon_m = \left[\frac{1}{3}\left(\frac{2}{\upsilon_T^3}+\frac{1}{\upsilon_L^3}\right)\right]^{-\frac{1}{3}} \qquad (10)$$

$$\upsilon_L = \sqrt{\frac{3B+4G}{3D}} \quad \text{and} \quad \upsilon_T = \sqrt{\frac{G}{D}}$$

where N_A is Avogadro's number, n is the number of atoms in the unit cell, M is the molecular weight, D is the density, υ_m is the mean sound velocity, υ_L is the longitudinal sound velocity and υ_T is the transversal sound velocity. The resulting values are listed in Table 5. Similar values of Young's moduli of (87±2) GPa and (80±5) GPa were also obtained for $Ba_{4.9}V_{12}Sb_{19.0}$ and $Ba_{4.9}Nb_{12}Sb_{19.4}$, respectively, if we take the Poisson's ratio of 0.22 from {Nb,Ta}Sb_2.[15] In that case the corresponding Debye temperatures calculated from Anderson's formulae are slightly higher (260 and 237 K).

Table 5. Elastic properties and Debye temperatures of $Ba_5\{V,Nb\}_{12}Sb_{19+x}$ and comparison of data obtained from different measurements

	H_V [GPa]	E_I [GPa]	ν*	G [GPa]	B [GPa]	CTE [$10^{-6}K^{-1}$]	θ_D [K]				θ_E [K]					
							ADP	C_p	ρ	E-moduli	ADP				C_p	
											$Ba1_{11}$	$Ba1_{22,33}$	Ba2	Sb7	θ_{E1}	θ_{E2}
$Ba_5V_{12}Sb_{19+x}$	4.1	85	0.26	33.7	59.0	15.8	229	247	247	254	73.2	89.6	81.8	67.9	72	40
$Ba_5Nb_{12}Sb_{19+x}$	3.6	79	0.26	31.3	54.9	14.9	206	235	235	233	66.3	78.3	72.5	-	70	41

*Taken from $V_{1-x}Sb_2$ [15]

4. Conclusions

This paper summarizes crystal structure analyses as well as the characterization of transport and mechanical properties of two novel compounds $Ba_5\{V,Nb\}_{12}Sb_{19+x}$. These compounds are variants of the stuffed γ-brass structure $Ba_5Ti_{12}Sb_{19+x}$. The disorder in these compounds leads to complicated and high values of electrical resistivity. Hardness measurements employing a nano-indenter revealed hardness values similar to filled Sb-based skutterudites, however, yield remarkably smaller Young's moduli of ~80 GPa. The atomic displacement parameters show rattling behavior for both Ba atoms in the V(Nb)-Sb framework, and (in case of $Ba_5V_{12}Sb_{19+x}$) additionally Sb7 in the octahedral cage formed by Ba1 atoms. The rattling behaviour in these compounds is reflected in various physical properties such as electrical resistivity, specific heat, and low thermal conductivity. $Ba_5Nb_{12}Sb_{19+x}$ possesses an extremely low lattice thermal conductivity, presumably close to the minimum thermal conductivity. A resistivity upturn at low temperatures occurs in both compounds, as well as a change from p- to n-type conductivity in $Ba_5Nb_{12}Sb_{19+x}$ above 300 K, suggesting the existence of a narrow gap in close proximity of the Fermi level.

Incompatibility of $Ba_5\{V,Nb\}_{12}Sb_{19+x}$ with Ba-filled Sb-based skutterudites in respect to a high coefficient of thermal expansion and dissimilar shear moduli together with the low thermal and electrical conductivity highly recommends to avoid formation of these phases in a hot contact zone between V,Nb electrodes and the skutterudite material.

5. Acknowledgement

The research reported herein was supported by the Austrian Federal Ministry of Science and Research (BMWF) under the scholarship scheme: Technology Grant Southeast Asia (Ph.D.) in the frame of the ASEA UNINET. Work supported in part by the Christian Doppler Laboratory for Thermoelectricity.

6. Notes

[a] *Institute of Materials Chemistry and Research, Faculty of Chemistry, University of Vienna, Währingerstraße 42, A-1090 Vienna, Austria. Email: fai.failamani@gmail.com, andriy.grytsiv@univie.ac.at, peter.franz.rogl@univie.ac.at; Fax: +43 142779524; Tel: +43 1427752456*

[b] *Institute of Physical Chemistry, University of Vienna, Währingerstraße 42, A-1090 Vienna, Austria. Email: fai.failamani@gmail.com, Fax: +43 142779524; Tel: +43 1427752456*

[c] *Institute of Mineralogy and Crystallography, University of Vienna, Althanstraße 14, A-1090 Vienna, Austria. Email: gerald.giester@univie.ac.at; Fax: +43 14277853235; Tel: +43 1427753235*

[d] *Research Group Physics of Nanostructured Materials, University of Vienna, Boltzmanngasse 5, A-1090 Vienna, Austria. Email: gerald.polt@univie.ac.at; michael.zehetbauer@univie.ac.at; Fax: 43 14277872843; Tel: +43 1427772843.*

[e] *Institute of Solid State Physics, Vienna University of Technology, Wiedner Hauptstraße 8-10, A-1040 Vienna, Austria. Email: heinrich@ifp.tuwien.ac.at; michor@ifp.tuwien.ac.at, bauer@ifp.tuwien.ac.at; Fax: +43 15880113199; Tel: +4315880113160*

[f] *Christian Doppler Laboratory for Thermoelectricity, Vienna, Austria.*

† Electronic Supplementary Information (ESI) available: [details of any supplementary information available should be included here]. See DOI: 10.1039/b000000x/

‡ Footnotes should appear here. These might include comments relevant to but not central to the matter under discussion, limited experimental and spectral data, and crystallographic data.

7. References

1 *Pauling File Binary Edition, Version 1.0, Release 2002/1*, ASM international, Materials Park, OH, USA, 2002.

2 P. Villars and K. Cenzual, *Pearson's Crystal Data–Crystal Structure Database for Inorganic Compounds, release 2014/15*, ASM International, Materials Park, OH, USA, 2014.

3 H. Bie and A. Mar, *J. Solid State Chem.*, 2009, **182**, 3131–3137.

4 G. Rogl, A. Grytsiv, K. Yubuta, S. Puchegger, E. Bauer, C. Raju, R. C. Mallik and P. Rogl, *Acta Mater.*, 2015, **95**, 201–211.

5 G. Schierning, R. Chavez, R. Schmechel, B. Balke, G. Rogl and P. Rogl, *Transl. Mater. Res.*, 2015, **2**, 025001.

6 G. Rogl, A. Grytsiv, P. Rogl, N. Peranio, E. Bauer, M. Zehetbauer and O. Eibl, *Acta Mater.*, 2014, **63**, 30–43.

7 G. Rogl, A. Grytsiv, P. Rogl, E. Bauer, M. Hochenhofer, R. Anbalagan, R. C. Mallik and E. Schafler, *Acta Mater.*, 2014, **76**, 434–448.

8 G. Rogl, A. Grytsiv, P. Heinrich, E. Bauer, P. Kumar, N. Peranio, O. Eibl, J. Horky, M. Zehetbauer and P. Rogl, *Acta Mater.*, 2015, **91**, 227–238.

9 G. J. Snyder and T. S. Ursell, *Phys. Rev. Lett.*, 2003, **91**, 148301.

10 X. Shi, J. Yang, J. R. Salvador, M. Chi, J. Y. Cho, H. Wang, S. Bai, J. Yang, W. Zhang and L. Chen, *J. Am. Chem. Soc.*, 2011, **133**, 7837–7846.

11 K. Bartholomé, IAV-Berlin, 2014.

12 G. Rogl and P. Rogl, *Sci. Adv. Mater.*, 2011, **3**, 517–538.

13 X. C. Fan, M. Gu, X. Shi, L. D. Chen, S. Q. Bai and R. Nunna, *Ceram. Int.*, 2015, **41**, 7590–7595.

14 D. Zhao, H. Geng and X. Teng, *J. Alloys Compd.*, 2012, **517**, 198–203.

15 F. Failamani, P. Broz, D. Macciò, S. Puchegger, H. Müller, L. Salamakha, H. Michor, A. Grytsiv, A. Saccone, E. Bauer, G. Giester and P. Rogl, *Intermetallics*, 2015, **65**, 94–110.

16 J. Rodriguez-Carvajal, *FULLPROF, a program for Rietveld refinement and pattern matching analysis, Abstract of the satellite meeting on powder diffraction of the XV congress, p. 127*, Int. Union of Crystallography, Talence, France, 1990.
17 W. Wacha, Diploma thesis, Technische Universität Wien, 1989.
18 C. C. D. Nonius Kappa, *DENZO SCALEPACK SORTAV Nonius Delft Neth.*, 1998.
19 G. M. Sheldrick, *Acta Crystallogr. A*, 2007, **64**, 112–122.
20 L. J. Farrugia, *J. Appl. Crystallogr.*, 1999, **32**, 837–838.
21 L. M. Gelato and E. Parthé, *J. Appl. Crystallogr.*, 1987, **20**, 139–143.
22 G. Schaudy, Diploma thesis, Technische Universität Wien, 1990.
23 G. Schaudy, Dissertation, Technische Universität Wien, 1995.
24 L. Leber, Diploma thesis, Technische Universität Wien, 2012.
25 L. Pauling and B. Kamb, *Proc. Natl. Acad. Sci. U. S. A.*, 1986, **83**, 3569–3571.
26 A. Junod, T. Jarlborg and J. Muller, *Phys. Rev. B*, 1983, **27**, 1568–1585.
27 M. Falmbigl, G. Rogl, P. Rogl, M. Kriegisch, H. Müller, E. Bauer, M. Reinecker and W. Schranz, *J. Appl. Phys.*, 2010, **108**, 043529.
28 M. Christensen, S. Johnsen and B. B. Iversen, *Dalton Trans.*, 2010, **39**, 978.
29 J. Callaway and H. C. von Baeyer, *Phys. Rev.*, 1960, **120**, 1149–1154.
30 J. Callaway, *Phys. Rev.*, 1959, **113**, 1046–1051.
31 J. Callaway, *Phys. Rev.*, 1961, **122**, 787–790.
32 D. G. Cahill, S. K. Watson and R. O. Pohl, *Phys. Rev. B*, 1992, **46**, 6131–6140.
33 A. I. Golovashkin, A. V. Gudenko, L. N. Zherikhina, M. L. Norton and A. M. Tskhovrebov, *J. Exp. Theor. Phys.*, 1994, **79**, 163–168.
34 S. Berger, Dissertation, Technische Universität Wien, 2003.
35 T. Chudoba, in *Nanostructured Coatings*, eds. A. Cavaleiro and J. T. M. D. Hosson, Springer New York, 2006, pp. 216–260.
36 O. L. Anderson, *J. Phys. Chem. Solids*, 1963, **24**, 909–917.